ELSEVIER

Polymer 41 (2000) 2183–2201

polymer

Constitutive model for the finite deformation stress–strain behavior of poly(ethylene terephthalate) above the glass transition

M.C. Boyce*, S. Socrate, P.G. Llana

Department of Mechanical Engineering, Massachusetts Institute of Technology, Cambridge, MA 02139-4307, USA

Received 12 March 1999; received in revised form 3 June 1999; accepted 4 June 1999

Abstract

A constitutive model for the finite deformation stress–strain behavior of poly(ethylene terephthalate) (PET) at temperatures above the glass transition temperature is presented. In this temperature regime, the behavior of PET is strongly dependent on strain rate and temperature; PET also experiences strain-induced crystallization at these temperatures. The constitutive model accounts for the rate and temperature dependence of the stress–strain behavior by modeling the competition between molecular orientation processes and molecular relaxation processes. The model is fully three-dimensional and is shown to be in good agreement with experimental data over a wide range in strain rates and temperatures as well as under both uniaxial compression and plane strain compression loading conditions.

Keywords: Poly(ethylene terephthalate); Stress–strain behavior; Glass transition temperature

1. Introduction

Poly(ethylene terephthalate) [PET]is often processed in the solid state at temperatures above its glass transition temperature by a variety of stretching processes (drawing, biaxial stretching, blow molding, vacuum forming). In many instances, the PET initial state is an isotropic amorphous state obtained via a rapid cooling from melt. The stretching processes act to impart a preferential orientation to the macromolecular network which, in turn, can result in strain-induced crystallization. Thus, the end product will be a material which is molecularly oriented and also partly crystalline. The level of molecular alignment and the percent crystallinity that develop with strain strongly depend on strain rate and temperature; the texture of the molecular orientation and the crystallinity also depend strongly on the mode of straining (e.g. uniaxial stretching vs. biaxial stretching). Specific aspects of the dependence of the stress–strain behavior on these parameters have recently been presented and discussed in some detail in the experimental work of Llana and Boyce [1]; other particularly relevant results are provided in Refs. [2–6].

Polymer stretching processes are often sequential and non-isothermal. For example, a film stretching process will typically consist of an axial stretch at one temperature followed by an orthogonal stretch at another temperature. Similarly, the blow molding process will first axially stretch the parison at one temperature and then pressurize it into the mold at another temperature. The strong dependence of the stress–strain behavior (and corresponding evolution in molecular orientation and crystallinity) on rate, temperature and mode of stretching, make the process and end product quality extremely sensitive to these processing parameters. Owing to the complexities of the dependencies of the material behavior and the complexities of the process itself, it is difficult to experimentally isolate and determine the magnitude of the effects that small variations in different process parameters can have on the end product. Accurate numerical modeling of the process using a technique such as the finite element method could provide valuable insight into the process physics and dependencies on various process parameters. In order to conduct such numerical studies, an accurate constitutive model of the strain rate and temperature dependent large strain stress–strain behavior of PET is required. In this paper, we address the development of a physically based internal state variable constitutive model of the stress–strain behavior of PET which captures the essential physics of the evolution in the underlying structure with strain, which in turn leads to the observed stress–strain behavior. In Section 2, we review specific features and dependencies of the stress–strain behavior of PET; in Section 3, we present the constitutive model formulation; and in Section 4, we present constitutive model results compared to experimental data.

* Corresponding author. Tel.: + 1-617-253-2342; fax: + 1-617-258-8742.

E-mail address: mcboyce@mit.edu (M.C. Boyce)

0032-3861/00/$ - see front matter
PII: S0032-3861(99)00406-1

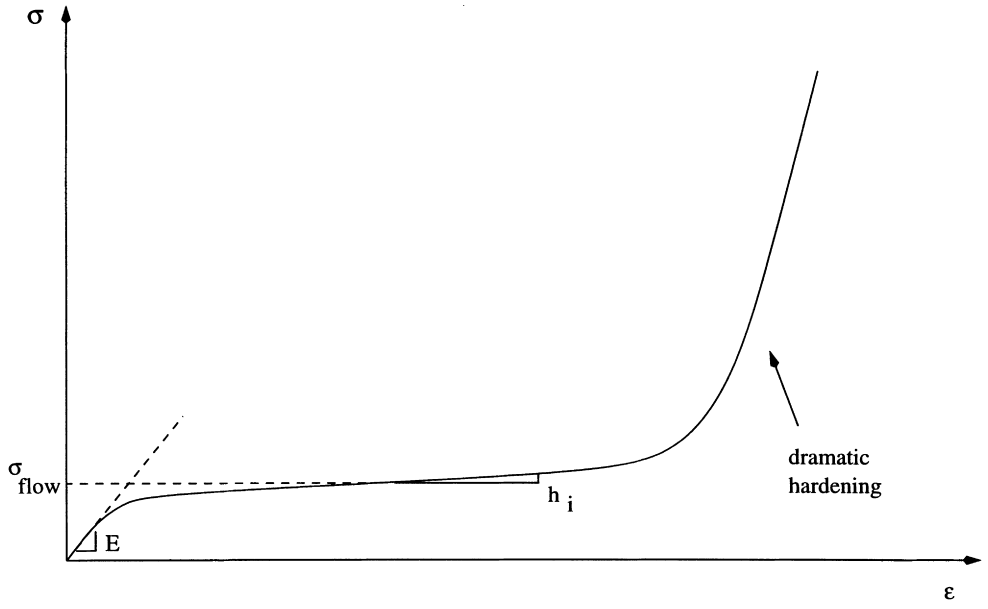

Fig. 1. Basic features of the stress–strain behavior of PET.

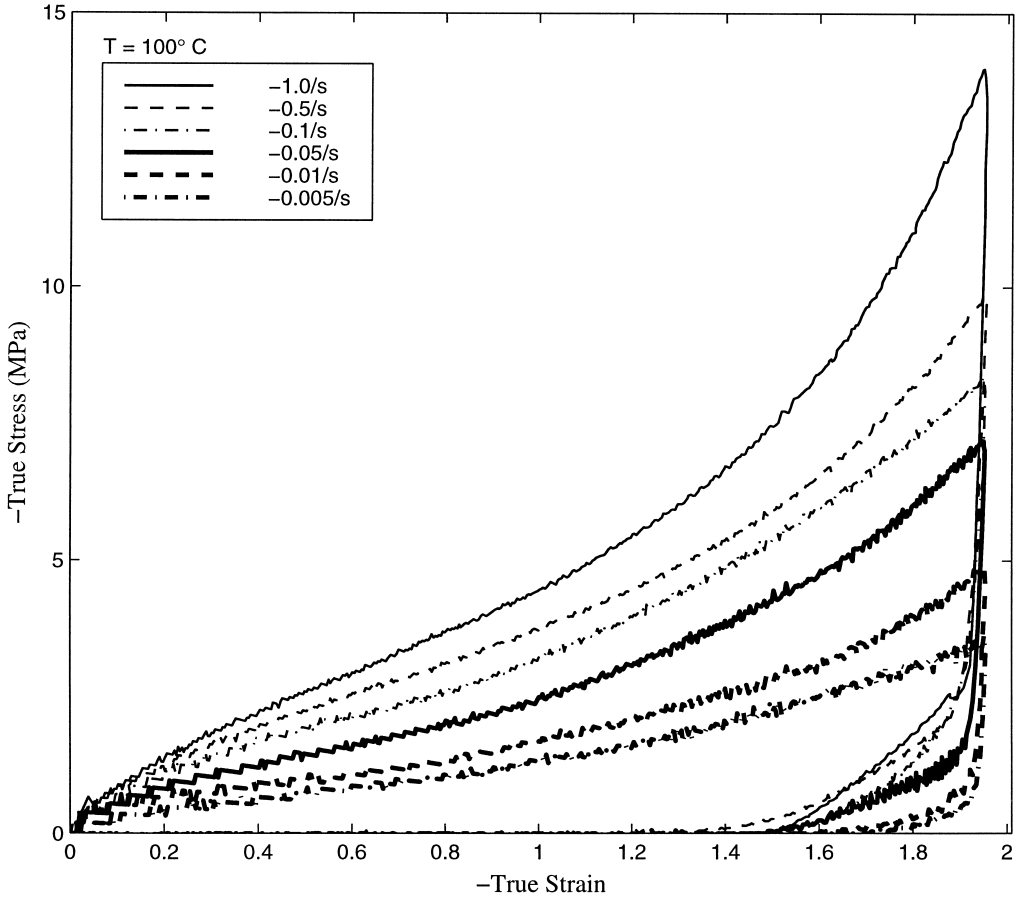

Fig. 2. Uniaxial compression stress–strain behavior of PET at 100°C, for strain rates between -1.0 and $-0.005\ s^{-1}$.

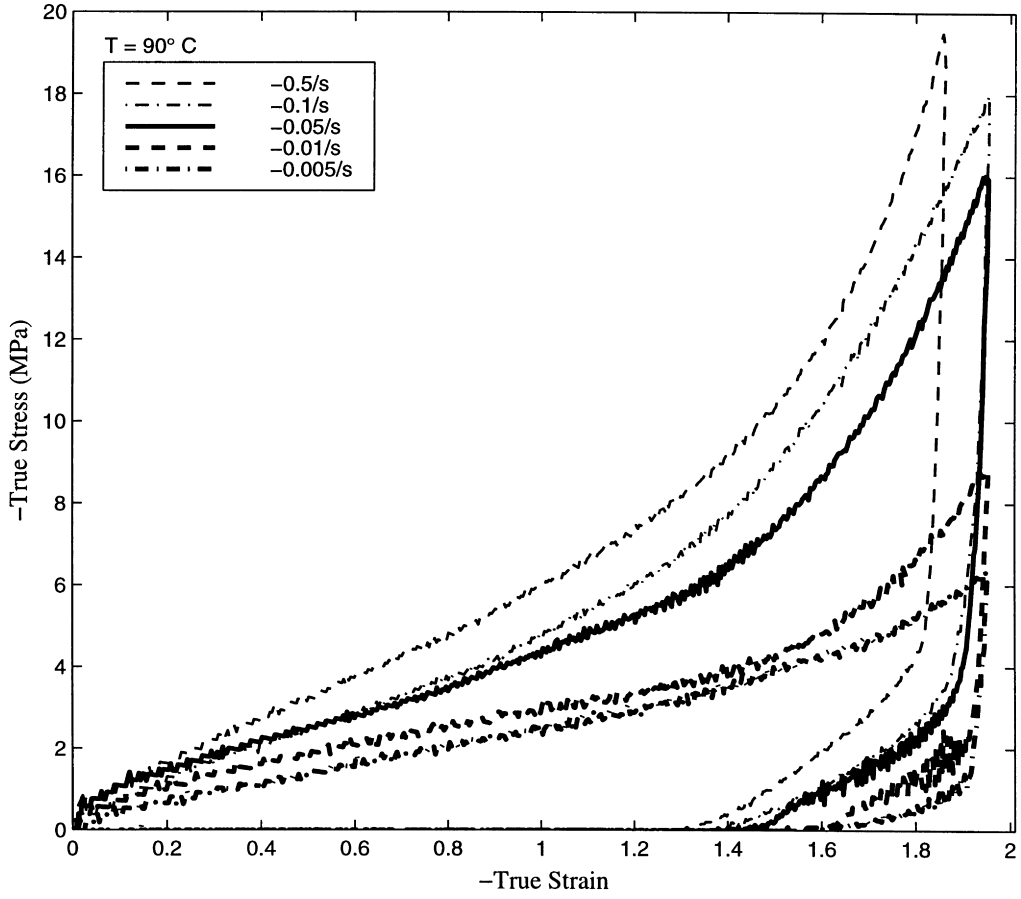

Fig. 3. Uniaxial compression stress–strain behavior of PET at 90°C, for strain rates between -0.5 and $-0.005\ s^{-1}$.

2. Aspects of experimentally observed stress–strain behavior

The stress–strain behavior of PET at temperatures above the glass transition temperature is observed to exhibit four basic features as shown in the schematic of Fig. 1. The stress–strain curve exhibits a relatively stiff initial response (with initial slope E), followed by a rollover to flow (σ_{flow}), followed by a steady increase in the stress with strain (with initial strain hardening/stiffening modulus h_i), followed by a dramatic increase in stress with strain at very large strains ("dramatic hardening" region). As shown immediately below, each of these features is found to depend on strain rate, temperature, and strain state.

Strain rate dependence. The strain rate dependence of the stress–strain behavior is shown in the Llana and Boyce [1] uniaxial compression data at 100°C in Fig. 2. Tests were conducted at a variety of constant strain rates to a true strain of -1.95. The initial stiffness is observed to exhibit a negligible dependence on strain rate. The rollover to flow is observed to occur at very low stress levels; however, the stress level of the rollover is observed to be rate dependent, increasing with an increase in strain rate. The initial hardening slope, h_i, is observed to be strongly rate dependent. The strain at which the transition to dramatic hardening takes place is also found to be strongly dependent on strain rate where lower rates (longer times) delay the upturn in the stress–strain curve. These same trends in behavior with strain rate have been observed at other temperatures [1]; experimental data for tests performed at 90°C are shown in Fig. 3. Similar strain rate dependence of the stress–strain behavior have recently been reported by Vigny et al. [7] in plane strain tension at 90°C.

Temperature dependence. The temperature dependence of the stress–strain behavior is shown in the uniaxial compression data at a strain rate of $0.1\ s^{-1}$ (Fig. 4) at temperatures of 90, 100, and 105°C. The initial stiffness, the flow stress, the initial strain hardening modulus, and the occurrence of dramatic hardening are all observed to be strongly temperature dependent. This temperature range is a typical range in which processing occurs. Clearly, small changes in temperature result in rather dramatic changes in mechanical behavior along with the corresponding changes in the evolution of the underlying microstructure. Similar temperature effects on the stress–strain behavior have been observed by Jabarin [2], Chandran and Jabarin [3], and Buckley et al. [4] in tensile stretching experiments.

State of strain dependence. The dependence of the stress–strain behavior on the state of imposed strain is illustrated in

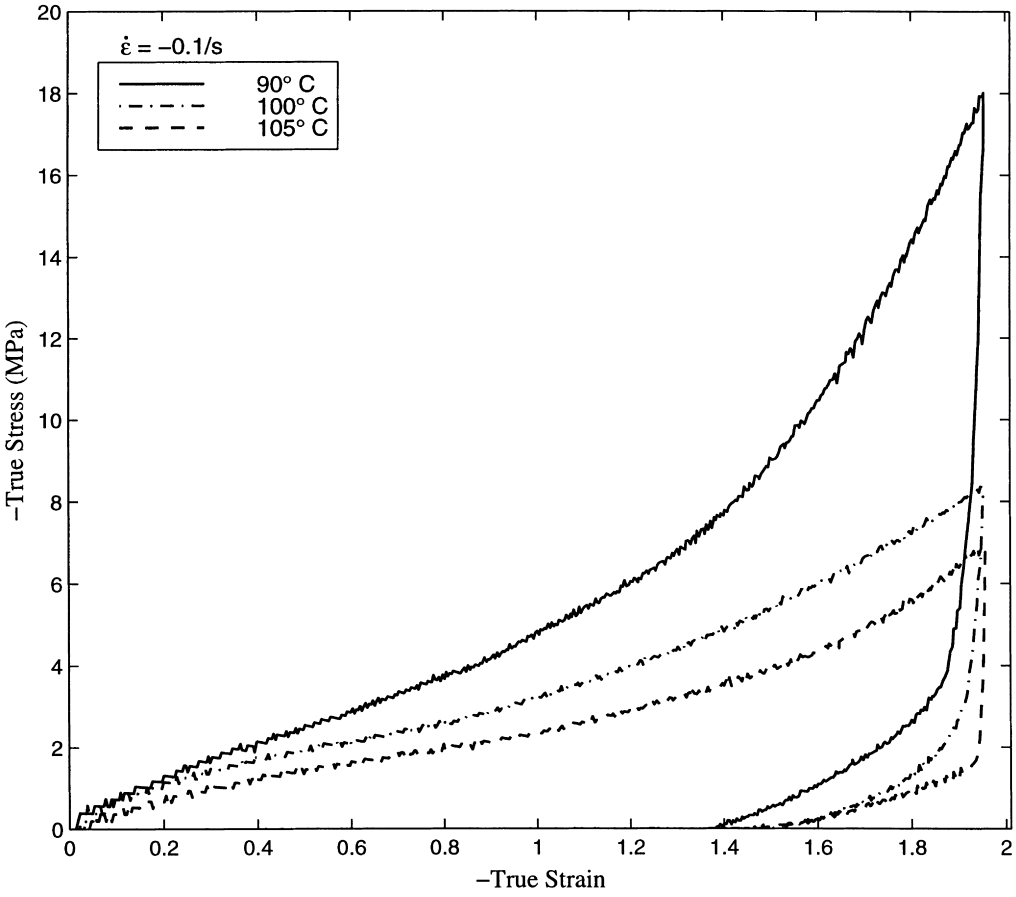

Fig. 4. Uniaxial compression stress–strain behavior of PET at temperatures of 90, 100, and 105°C, for a strain rate of $-0.1\ s^{-1}$.

Fig. 5 where the uniaxial compression and plane strain compression stress–strain curves at three strain rates are shown at 100°C. The plane strain stress–strain data exhibits the same strain rate dependence of flow stress, initial strain hardening slope, and dramatic hardening upturn as was observed in Fig. 2 for uniaxial compression. Comparison of the uniaxial compression and plane strain compression data at any given strain rate shows the strong dependence of flow stress, initial strain hardening and dramatic hardening on state of strain. The state of strain dependence of the flow stress behavior can be explained in terms of examination of the equivalent stress at flow using a Mises yield condition. The initial strain hardening slope and the dramatic upturn in strain hardening follow the basic dependencies found for glassy polymers as detailed in Ref. [8], where the dependence of strain hardening on state of strain was found to be due to the nature of the development in molecular orientation with different modes of straining. In the data of Fig. 5, the PET strain hardening behavior appears to be even more dramatic than the hardening behavior observed in the glassy polymers studied by Arruda and Boyce. The more dramatic upturns observed in PET are associated with the occurrence of strain-induced crystallization in PET where Llana and Boyce measure large increases in crystallinity content after strain levels of −1.0, consistent with reports of other investigators. The development of strain-induced crystallization was also found to be highly dependent on the state of strain; plane strain deformation provides better conditions for crystallization because the unidirectionality of the molecular network orientation promotes the structural order favorable for crystallization. These aspects of the connections between molecular orientation and strain-induced crystallization will be discussed in more detail in Section 3.[1]

Unloading behavior. The unloading behavior is highly non-linear for all strain rates and temperatures as shown

[1] Note that at some of the higher rates, adiabatic heating would be expected to play a role. A first order analysis indicates a minimal rise in temperature due to plastic dissipation. However, crystallization is an exothermic process and therefore the material temperature should be increasing during strain-induced crystallization. Temperature measurements were not taken, but differential scanning calorimetry exotherms were used to estimate a value for the temperature rise to be approximately 15°C, which obviously impacts the mechanical behavior. However, thermal softening is never directly observed in the stress–strain curve due to the simultaneous occurrence of thermal softening with strong strain hardening from crystallization. Clearly, care must be taken when interpreting these complex material state issues. Furthermore, the occurrence of strain-induced crystallization is also found to be rate dependent, where more crystallization is found to occur at higher rates as is consistent with the observed stress–strain behavior where more strain hardening is observed at higher rates.

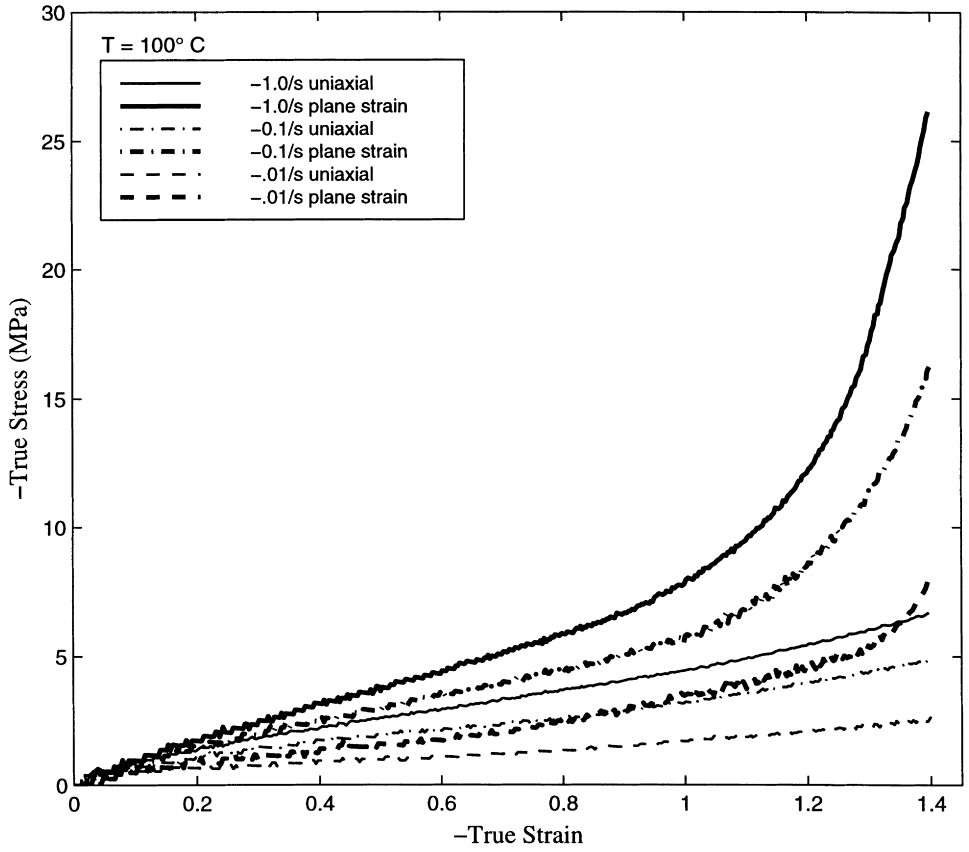

Fig. 5. Plane strain compression and uniaxial compression stress–strain behavior of PET at 100°C, for strain rates of -1.0, -0.1, and $-0.01\ s^{-1}$.

in Figs. 2–4. The unloading response is initially linear, with a stiffness larger than the initial stiffness observed during loading. The response takes on a non-linear character after a magnitude in stress reversal that depends on rate, temperature and strain. For all of the experimental curves, the residual strain is significant, with a strain recovery, which depends on rate, temperature and strain.

3. Constitutive model development

The stress–strain behavior can be interpreted as a response to overcoming two basic resistances to deformation: (1) an intermolecular barrier to deformation which is further augmented by the occurrence of strain-induced crystallization; and (2) an evolving anisotropic resistance due to molecular orientation. The first resistance results in the initially stiff response as well as the rate and temperature dependence of initial flow; this resistance is taken to increase due to the strain-induced crystallization. The second resistance produces the anisotropic strain hardening/stiffening behavior resulting from molecular alignment. This fundamental breakdown of the deformation resistance is depicted schematically in Fig. 6 and conceptually follows the basic framework proposed for amorphous polymers in Ref. [9] as well as in Ref. [10], where the work of Boyce

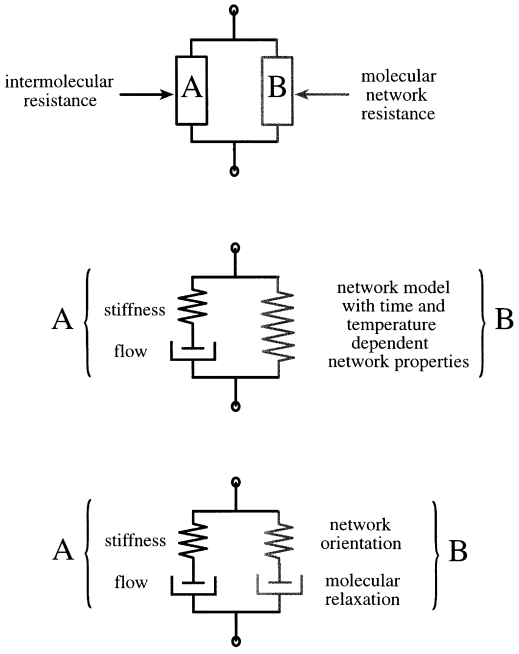

Fig. 6. (a) Schematic representation of the breakdown of the total resistance into an intermolecular resistance occurring in parallel with a network resistance. (b) Elastic–viscoplastic representation of the intermolecular resistance acting in parallel with a time and temperature dependent network. (c) The network resistance is modeled as a network orientation process and a molecular relaxation process acting together to accommodate deformation.

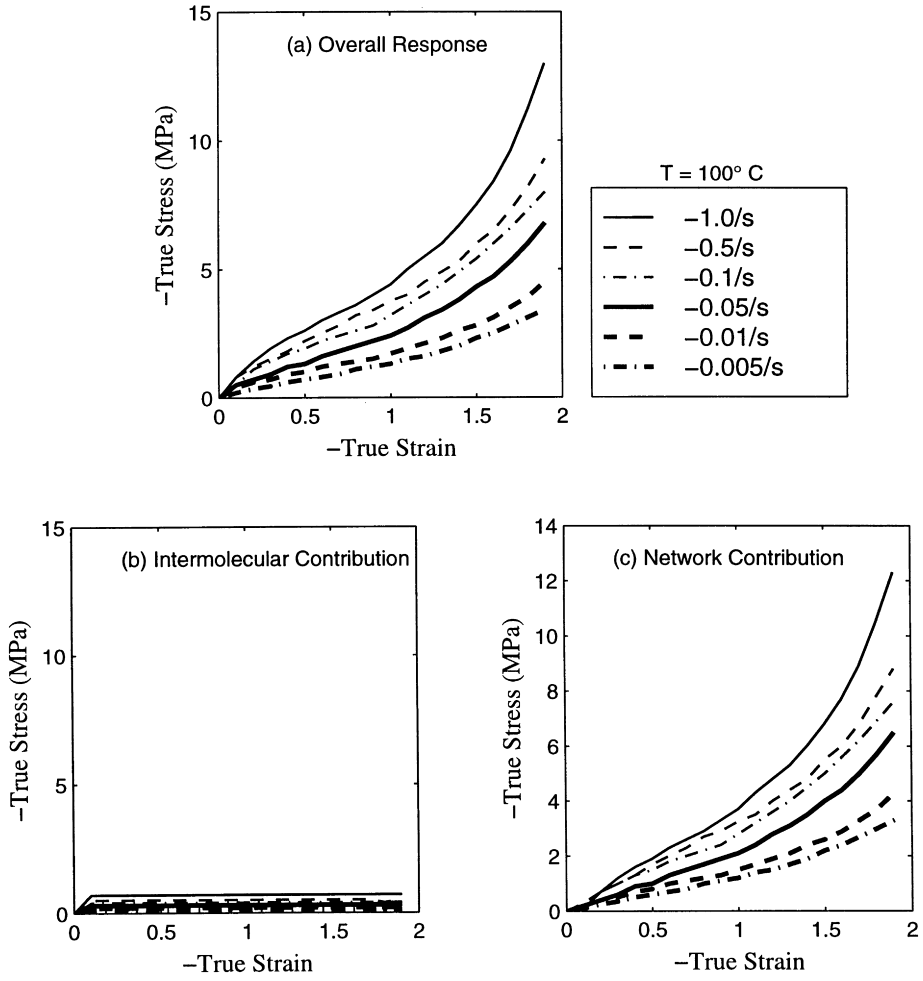

Fig. 7. Interpretation of the overall stress–strain response of PET at 100°C (a), in terms of an intermolecular contribution (b), and a network contribution (c).

et al. also provided a general three-dimensional finite strain formalism. Buckley and Jones [11] also consider a similar breakdown in their modeling of PET behavior.[2] In the following sections, the experimental data is first interpreted in terms of the two basic resistances; a mathematical representation of the proposed model is then provided.

3.1. Interpretation of data in terms of physics of deformation

Using the conceptual framework of two resistances (an intermolecular resistance and a molecular orientation resistance) acting in parallel, the development of a physically based constitutive model for the stress–strain behavior of PET can now begin with an interpretation of the data discussed in Section 2. The data is interpreted below in terms of a series of four conceptual steps.

Step 1 (isolation of initial stiffness and initial flow stress). The initial portion of the stress–strain curve displays a relatively stiff response followed by flow. The initial stiffness is found to be dependent on temperature, but only weakly dependent on strain rate; the flow stress is found to be dependent on both strain rate and temperature. This behavior is similar to that observed in glassy polymers albeit the stiffness and flow stress are at least an order of magnitude lower in the PET above the glass transition temperature, θ_g than that observed in a glassy state polymer. Note that $\theta_g = 79$°C for this material. The similarity in the initial response suggests capturing this initial behavior in a manner similar to Boyce et al. [10] where the initial stiffness is modeled with a three-dimensional linear elastic spring and the rate and temperature dependent flow is modeled as a thermally activated process. Physically, the initial stiffness probes intermolecular interactions and the flow stress is the stress level required to overcome intermolecular barriers to deformation. At these high temperatures, the intermolecular barriers are low and therefore the flow stress levels are low compared to those observed in the glassy state.

Step 2 (strain hardening/stiffening behavior). Taking the 100°C uniaxial data of Fig. 2 as the working example, the

[2] Note that the Buckley and Jones work does not provide a completely general three-dimensional formulation, but is presented in terms of principal stretch space only. Also, the Buckley and Jones work uses an unusual elastic–plastic decomposition of the deformation gradient $\Lambda = \Lambda^p \Lambda^e$ instead of the more conventional $\mathbf{F} = \mathbf{F}^e\mathbf{F}^p$.

initial stiffness and flow stress can be isolated and then subtracted from the overall stress–strain behavior as illustrated in Fig. 7. The remaining portion of the stress–strain behavior is the strain hardening/stiffening behavior shown in Fig. 7(c). The rate dependence of strain hardening at 100°C is thus clearly identified in the reduced data of Fig. 7(c). A similar exercise can be performed on data at different temperatures to characterize the temperature dependence of strain hardening. The exercise can also be performed on the plane strain data. This breakdown of the stress–strain behavior is conceptually illustrated in the analog model of Fig. 6 where the initial resistance to flow (obtained in Step 1) acts in parallel to the strain hardening/stiffening behavior (obtained in Step 2).

Figs. 2–5 illustrate the strong strain rate, temperature, and strain state dependence of the strain hardening/stiffening behavior. The overall shape of the strain hardening behavior as well as the nature of its strong dependence on state of strain is analogous to the strain-hardening behavior observed in glassy polymers. This suggests that the PET hardening behavior is primarily governed by the orientation of the underlying macromolecular network and not necessarily so much by the occurrence of strain-induced crystallization. Therefore, in a first attempt, the hardening behavior could be modeled by the Arruda–Boyce network model of rubber-elasticity which has been found to accurately capture the state of strain dependence of the stress–strain behavior of elastomers and glassy polymers. Zaroulis and Boyce [12] had also verified the ability of the Arruda–Boyce model to capture the strain hardening of PET at temperatures in the glass transition region, however the hardening was not significantly rate or temperature dependent at those temperatures. Adams and Buckley [5] and Buckley et al. [4] modeled the hardening behavior of PET at temperatures above θ_g using a rubber-elasticity model, the Edwards–Vilgis model [13], again illustrating that the basic hardening behavior can be captured using a network orientation representation. However, network orientation models do not exhibit the rate and temperature dependent aspects observed in PET above θ_g. Indeed, the results of Buckley et al. also specifically demonstrated the inability of a rubber–elastic network model to capture the strong temperature dependence of hardening observed at these temperatures in PET.

In order to capture the rate and temperature dependent aspects of the hardening behavior, some modification must then be incorporated into network models. In an attempt in this direction, Arruda et al. [14] had observed temperature dependent hardening in PMMA and were able to successfully capture this dependence by using a network model where the network parameters (the chain density, n, and the number of units between entanglements, N) were temperature dependent. This approach is physically justified because, as the temperature is increased, some entanglements will become ineffective and n will decrease (thus acting to decrease the initial hardening modulus) and N will increase (thus acting to increase the strain at which the dramatic upturn in hardening occurs). Their product, nN, is taken to remain constant in order to conserve mass. In a very recent work by Vigny et al. [7], a similar approach is taken on PET at 90°C to account for the rate dependence of hardening, where the Arruda–Boyce rubber-elasticity model was used as the base network model. The approach adopted by Arruda et al. [14] and Vigny et al. [7] is thus one where the time and temperature dependence of the network response is captured through a time and temperature dependence of the network properties.

An alternative approach to capturing the time and temperature dependence of the network behavior was proposed in Ref. [4] whereby they propose to decompose the total deformation into a portion which goes to orienting the network and a portion which is accommodated by time and temperature dependent molecular relaxation.[3] No details on implementation of this decomposition were given in [4]. Recent work by the same group [15] shows success in capturing the temperature dependence of strain hardening using the proposed decomposition of deformation approach, but again no specific constitutive formulation is provided. This decomposition approach is attractive due to its potential ease in accommodating non-isothermal loading conditions such as a temperature history during stretching. The underlying physical basis of this approach lies in the existence of some basic macromolecular network which orients with deformation; however, at these high temperatures, if given enough time, molecular relaxation will accommodate some of the imposed deformation and thus only a portion of the deformation goes to actual orientation of the network. The Arruda, Boyce and Jayachandran approach accounts for the molecular relaxation in terms of the properties of the network instead of an allocation of the imposed deformation. The two approaches are compared in the schematic of Fig. 6. The decomposition approach appears to provide a higher degree of flexibility in terms of its ability to handle various temperature loading histories, and it will be adopted here as discussed next in Step 3.

Step 3 (isolation of molecular orientation and molecular relaxation contributions to hardening response). Data in Fig. 2–5 had demonstrated the strong strain rate and temperature dependence of the strain hardening behavior in uniaxial compression. Further comparison of the strain hardening behavior at 90°C at the high rate of $-0.5\ s^{-1}$ with that at 80°C at $-0.5\ s^{-1}$ (see [17]) finds these behaviors to be similar indicating that there is little molecular relaxation contribution in the 90°C, $-0.5\ s^{-1}$ data. Therefore, the 90°C, $-0.5\ s^{-1}$ strain hardening behavior can be approximated to represent the molecular orientation contribution to the strain hardening behavior. This data can then be used to distinguish the portion of the imposed strain, which acts to orient the network from the portion, which is accommodated by molecular relaxation over the range in strain

[3] A similar decomposition was used recently in Ref. [16] to capture time and hysteresis aspects of the mechanical behavior of elastomers.

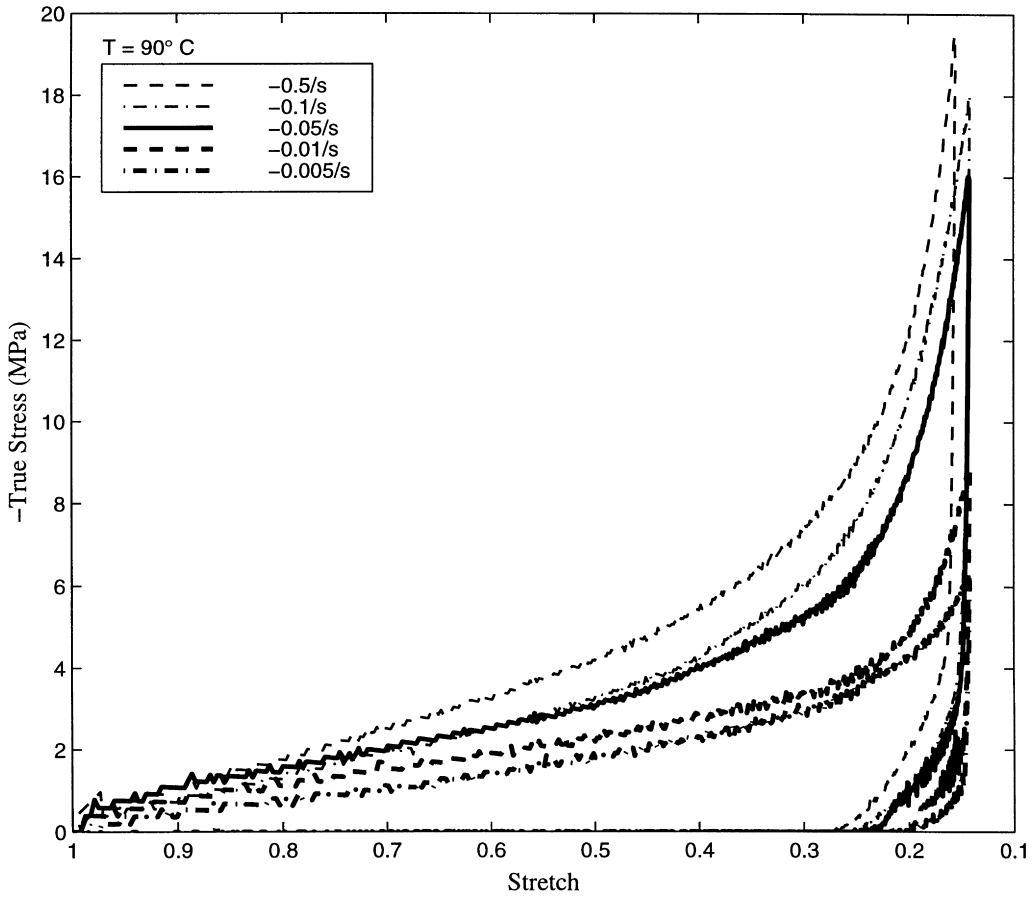

Fig. 8. Uniaxial compression stress–stretch behavior of PET at 90°C, for strain rates between -0.5 and $-0.005\ s^{-1}$.

rates and temperatures. For example, in the 90°C data of Fig. 3, the strain hardening behavior at a strain rate of $-0.5\ s^{-1}$ exhibits a stress magnitude of -4 MPa at a strain of -0.60 but at the lower rate of $-0.01\ s^{-1}$, it does not reach -4 MPa until a strain of -1.4. Since a network strain of only -0.60 is required to produce the stress of -4 MPa, a significant portion of the -1.4 strain imposed at the rate of $-0.01\ s^{-1}$ must be accommodated by molecular relaxation. Thus, the decomposition of the imposed strain into molecular relaxation contributions and molecular orientation contributions can be quantified by careful reduction of the data.

Large strain deformation is best decomposed in terms of a deformation quantity such as the deformation gradient or the stretch. In order to decompose the strain hardening behavior into its two contributions, the 90°C strain hardening stress–strain behavior is replotted in Fig. 8 in terms of corresponding stress–stretch curves. Using the $-0.5\ s^{-1}$ behavior as the basic molecular orientation contribution, the orientation stretch (to be called the network stretch) as a function of imposed stretch at the different rates can be plotted (Fig. 9(a)). Using a multiplicative decomposition of the total axial stretch into network and flow stretches ($\lambda = \lambda^N\lambda^F$), the flow stretch (the molecular relaxation contribution) can also be plotted as a function of imposed stretch (Fig. 9(b)). The flow stretch is observed to monotonically increase with imposed stretch, and eventually level off. More stretch is accommodated by flow at lower strain rates. A cross plot of the flow stretch as a function of the network stretch (Fig. 9(c)) suggests that, in uniaxial compression at 90°C, the flow stretch levels off or ceases after a network stretch between 0.6 and 0.5 is reached.

Construction of network and flow stretch history plots for the 100°C data (Fig. 10(a) and (b)) show similar results. The flow stretch monotonically increases with imposed stretch, where flow eventually levels off after different amounts of imposed stretch depending on the rate and temperature. The flow stretch vs. network stretch plots indicate that flow (molecular relaxation) ceases after a network stretch between 0.6 and 0.35 in uniaxial compression at all three temperatures and all strain rates. These results suggest that after sufficient molecular orientation, the structure resists relaxation. These stretch levels appear to roughly correspond to the onset of strain-induced crystallization. These data are in agreement with the Buckley group observation that there is an arrest in viscous flow which is temperature dependent [15] and this arrest correlates with network stretching. The data of Figs. 9 and 10 demonstrated both the rate and temperature dependence of this arrest in flow. These data will be used later in the construction of the mathematical model.

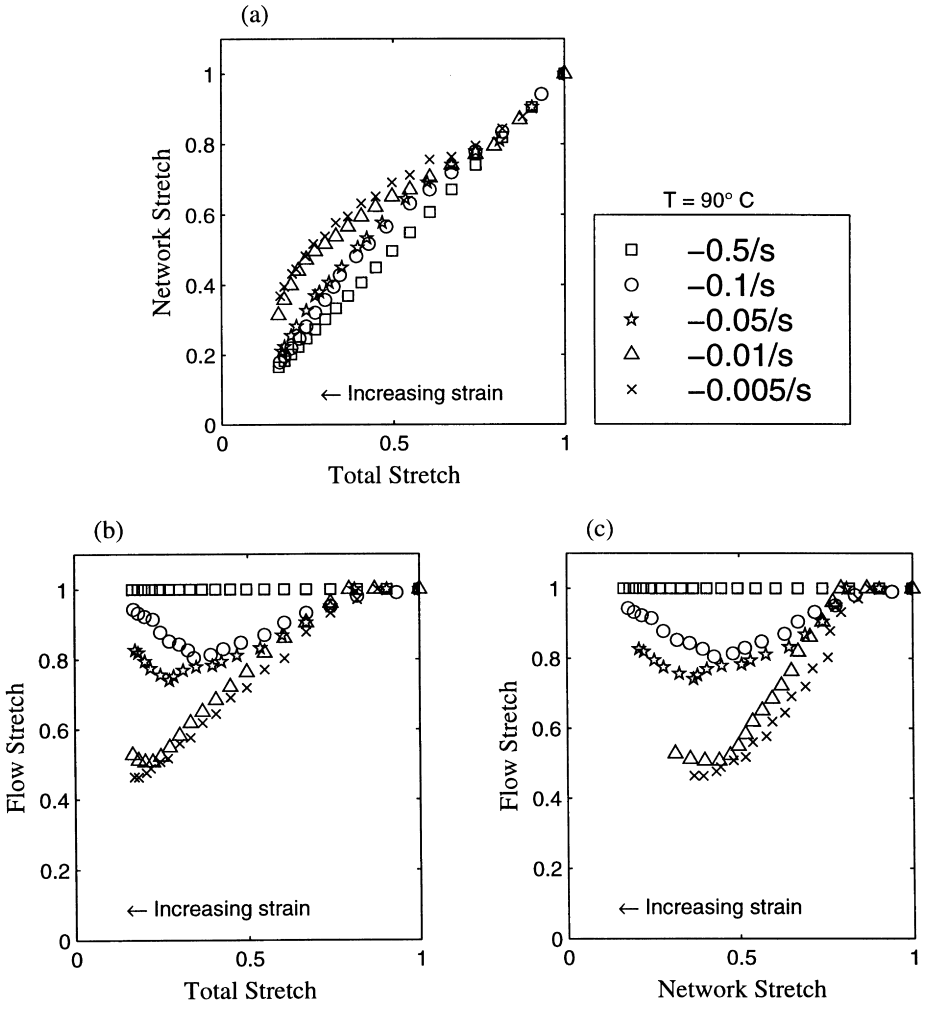

Fig. 9. Relations between total stretch, network stretch and flow stretch at 90°C, in uniaxial compression: (a) network stretch vs. applied stretch; (b) flow stretch vs. applied stretch; (c) flow stretch vs. network stretch.

Step 4 (inclusion of strain-induced crystallization effects). As the molecular network orients with strain, the orientation acts to provide a structure amenable to crystallization due to the nature of the PET backbone and the high temperature of the deformation. Strain-induced crystallization is thought to provide a second strain hardening mechanism in addition to that of molecular orientation as will be discussed in the mathematical model construction. As importantly, the occurrence of strain-induced crystallization acts to lock-in the highly oriented structure and leads to the extensive permanent deformation observed upon unloading. The effect of strain-induced crystallization on the recovery process will be explored in the mathematical model construction.

3.2. Mathematical model formulation

The mathematical representation of the constitutive model is based on the analog representation of the breakdown of the overall deformation resistance into an intermolecular resistance (resistance A) acting in parallel with a network resistance (resistance B) depicted in Fig. 6(c). The model first recognizes that the deformation gradient acting on each resistance is equal to the imposed deformation gradient, **F**

$$\mathbf{F}_A = \mathbf{F}_B = \mathrm{F}, \tag{1}$$

where $\mathbf{F} = \nabla_x \mathbf{p}$ with **p** being the current position of a material point and **x** the original position.

Then, following a method similar to that given in Ref. [16], the behavior of each resistance is separately formulated. In all that follows, symbols in lower case italics indicate scalar quantities; symbols in lower case bold indicate vector quantities; symbols in upper case bold indicate second order tensors, and any exception will be specifically noted.

3.2.1. Resistance A: intermolecular resistance

The initial stiffness of the overall behavior and also the rate and temperature dependence of the flow stress are shown in the data reduction of Fig. 7(b) and are considered to be governed by intermolecular barriers to deformation.

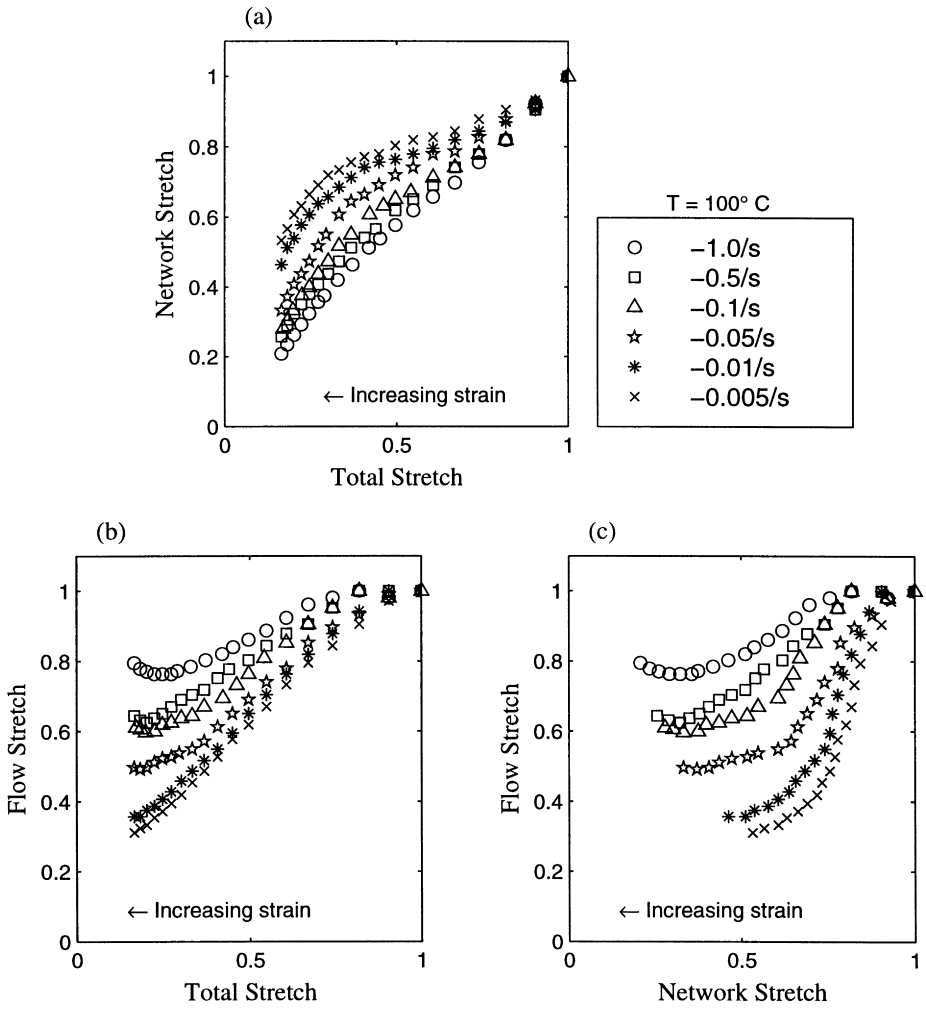

Fig. 10. Relations between total stretch, network stretch and flow stretch at 100°C, in uniaxial compression: (a) network stretch vs. applied stretch; (b) flow stretch vs. applied stretch; (c) flow stretch vs. network stretch.

This behavior of an initially stiff response followed by flow is represented in the analog model as a spring in series with a viscous element. The spring represents the initially stiff elastic response due to van der Waal interactions with surrounding molecules. Once the stress level reaches a critical level, the energy barrier to molecular chain segment rotation is overcome and flow ensues. The deformation can therefore be decomposed into elastic and plastic components via the multiplicative decomposition of the deformation gradient:

$$\mathbf{F}_A = \mathbf{F}_A^e \mathbf{F}_A^p, \tag{2}$$

where $\mathbf{F}_A^e$ and $\mathbf{F}_A^p$ can be further decomposed into stretch and rotation components

$$\mathbf{F}_A^e = \mathbf{V}_A^e \mathbf{R}_A^e, \qquad \mathbf{F}_A^p = \mathbf{V}_A^p \mathbf{R}_A^p. \tag{3}$$

The corresponding rate kinematics begin with the velocity gradient of resistance A

$$\mathbf{L}_A = \dot{\mathbf{F}}_A \mathbf{F}_A^{-1}, \tag{4}$$

which can be decomposed into elastic and plastic contributions

$$\mathbf{L}_A = \dot{\mathbf{F}}_A^e \mathbf{F}_A^{e-1} + \mathbf{F}_A^e \dot{\mathbf{F}}_A^p \mathbf{F}_A^{p-1} \mathbf{F}_A^{e-1} = \mathbf{L}_A^e + \tilde{\mathbf{L}}_A^p, \tag{5}$$

where $\tilde{\mathbf{L}}_A^p = \tilde{\mathbf{D}}_A^p + \tilde{\mathbf{W}}_A^p$. The unloaded configuration can be made unique through various approaches [18]; one convenient approach is to prescribe the spin $\tilde{\mathbf{W}}_A^p = 0$. This prescription will, in general, result in elastic and plastic deformation gradients which include rotations.

The rate of plastic stretching $\tilde{\mathbf{D}}_A^p$ must be constitutively prescribed

$$\tilde{\mathbf{D}}_A^p = \dot{\gamma}_A^p \mathbf{N}_A, \tag{6}$$

where $\mathbf{N}_A$ is the normalized deviatoric stress acting on element A

$$\mathbf{N}_A = \frac{1}{\sqrt{2}\tau_A} \mathbf{T}'_A, \qquad \tau_A = \left[\tfrac{1}{2} \mathbf{T}'_A \mathbf{T}'_A \right]^{1/2} \tag{7}$$

and $\mathbf{T}_A$ is constitutively related to the elastic deformation

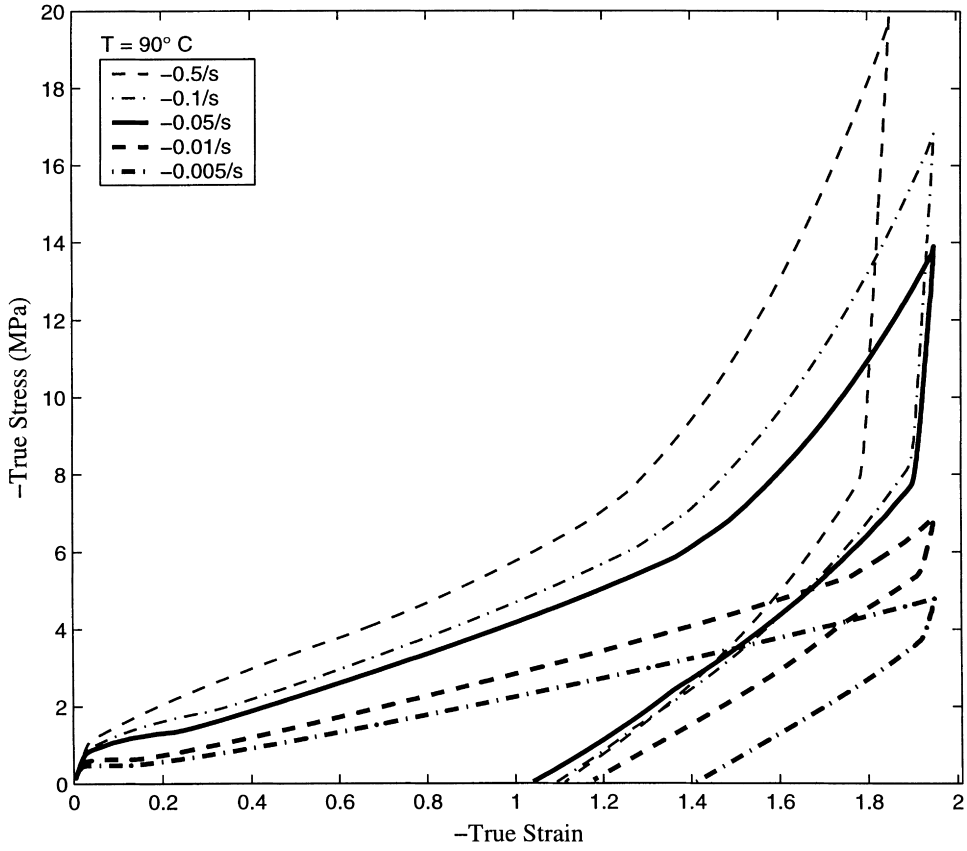

Fig. 11. Model predictions for the stress–strain behavior of PET at 90°C in uniaxial compression.

gradient by

$$\mathbf{T}_A = \frac{1}{J_A}\mathscr{L}^e[\ln \mathbf{V}_A^e], \tag{8}$$

where $J_A = \det \mathbf{F}_A^e$ is the volume change, $\mathscr{L}^e$ is the fourth order tensor of elastic constants, and $\ln \mathbf{V}_A^e$ is the Hencky strain. The constitutive description for the rate of plastic straining $\tilde{\mathbf{D}}_A^p$ is completed by the constitutive relation for the plastic strain rate $\dot{\gamma}_A^p$. Here, the rate of flow is taken to follow a thermally activated process [19] in a manner similar to that used in Ref. [10]

$$\dot{\gamma}_A^p = \dot{\gamma}_{0A} \exp\left[-\frac{\Delta G(1-\tau_A/s)}{k\theta}\right], \tag{9}$$

where $\dot{\gamma}_{0A}$ is the pre-exponential factor, ΔG the energy barrier to flow, s the shear resistance taken to be $0.15G$[4] where G is the elastic shear modulus, k the Boltzmann constant, and θ is the absolute temperature. Eqs. (1)–(9) completely describe the kinematic and constitutive aspects of the deformation resistance A. Eq. (9) will be revisited later in order to address influences of strain-induced crystallization on resistance A.

[4] The shear resistance can be further modified to account for pressure dependence as shown in Ref. [10].

3.2.2. Resistance B: network resistance

The deformation acting on the network element "B" is taken to be accommodated by two mechanisms: (i) the stretching/orientation of the underlying molecular network and (ii) molecular relaxation. These two mechanisms are represented in the analog model of Fig. 6(c) as a non-linear spring (the network orientation spring) acting in series with a viscous element (the molecular relaxation). The deformation gradient $\mathbf{F}_B$ can therefore be decomposed into network orientation ($\mathbf{F}_B^N$) and flow ($\mathbf{F}_B^F$) gradients in a manner similar to the elastic–plastic decomposition of the deformation gradient

$$\mathbf{F}_B = \mathbf{F}_B^N \mathbf{F}_B^F, \tag{10}$$

where $\mathbf{F}_B^N$ and $\mathbf{F}_B^F$ can be further decomposed into stretch and rotation components as had been done for $\mathbf{F}_A$ in Eq. (3). The corresponding rate kinematics for resistance B follow those given earlier for resistance A

$$\begin{aligned} &\mathbf{L}_B = \dot{\mathbf{F}}\mathbf{F}_B^{-1}, \\ &\mathbf{L}_B = \dot{\mathbf{F}}_B^N \mathbf{F}_B^{N-1} + \mathbf{F}_B^N \dot{\mathbf{F}}_B^F \mathbf{F}_B^{F-1} \mathbf{F}_B^{N-1} = \mathbf{L}_B^e + \tilde{\mathbf{L}}_B^F, \end{aligned} \tag{11}$$

where $\tilde{\mathbf{L}}_B^F = \tilde{\mathbf{D}}_B^F + \tilde{\mathbf{W}}_B^F$. Again, as in the rate formulation for resistance A, the spin $\tilde{\mathbf{W}}_B^F = \mathbf{0}$. The rate of molecular relaxation $\tilde{\mathbf{D}}_B^F$ will be constitutively prescribed later.

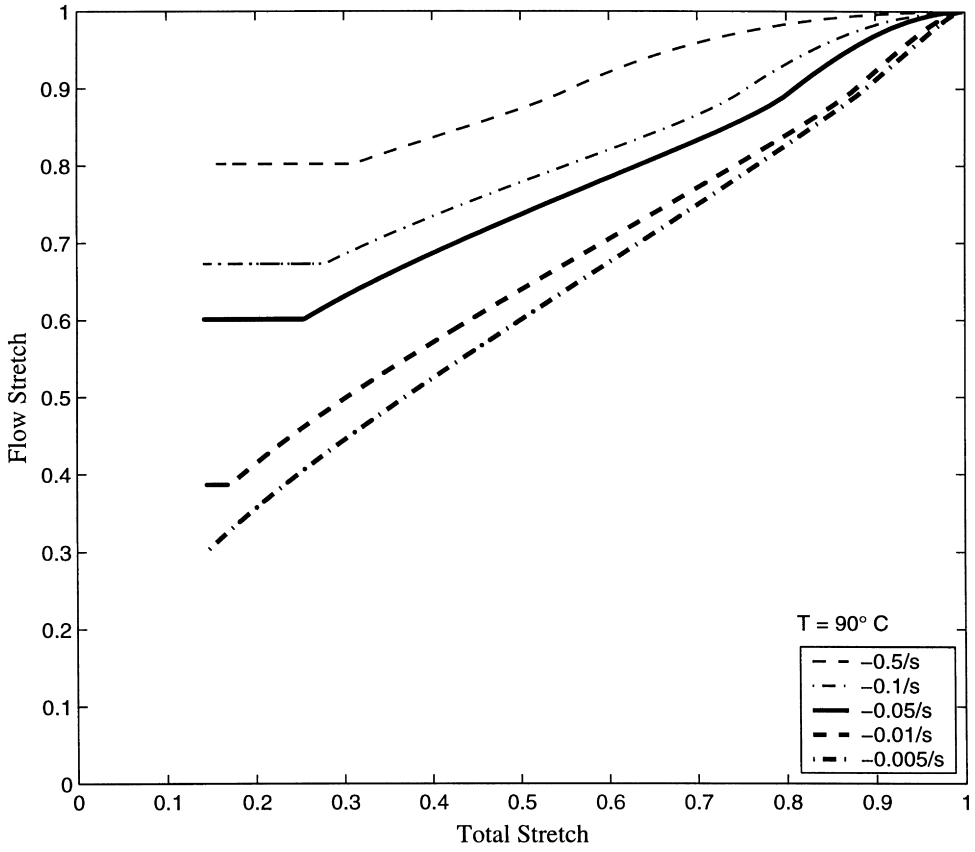

Fig. 12. Model predictions for the evolution of flow stretch with applied stretch at 90°C in uniaxial compression.

The stress arising from the network resistance is determined by the network orientation which is prescribed by the Arruda–Boyce eight-chain rubber-elasticity model [22]. This model is based on an eight-chain network of non-Gaussian chains. During deformation, each chain is found to stretch and rotate with deformation. The stretch on each chain in the network, $\bar{\lambda}_N$, is given by the root mean square of the distortional applied stretches $\bar{\lambda}_N = [\frac{1}{3}\mathrm{tr}(\bar{\mathbf{B}}^N)]^{1/2}$ where $\bar{\mathbf{B}}^N = \bar{\mathbf{F}}^N_B \bar{\mathbf{F}}^{NT}_B$, and $\bar{\mathbf{F}}^N_B = (J_B)^{-1/3}\mathbf{F}^N_B$ where $J_B = \det \mathbf{F}^N_B$. The stress–stretch relation is given by

$$\mathbf{T}_B = \frac{1}{J_B}\frac{nk\theta}{3}\frac{\sqrt{N}}{\bar{\lambda}_N}\mathscr{L}^{-1}\left[\frac{\bar{\lambda}_N}{\sqrt{N}}\right][\bar{\mathbf{B}}^N - (\bar{\lambda}_N)^2\mathbf{I}], \tag{12}$$

where n is the chain density and N the number of "rigid links" between entanglements. The quantity $nk\theta$ is proportional to the initial hardening modulus of the network orientation portion of the strain hardening curve, (i.e. the 90°C, $-0.5\ \mathrm{s}^{-1}$ data of Fig. 3) and N is determined from the strain level of the dramatic upturn in the strain hardening curve. $\mathscr{L}^{-1}$ is the inverse Langevin function given by $\mathscr{L}(\beta) = \coth(\beta) - (1/\beta)\mathscr{L}^{-1}[\bar{\lambda}_N/\sqrt{N}]$ provides the functionality that as $\bar{\lambda}_N$ approaches $\sqrt{N}$, the stress begins to rise dramatically.

The rate of molecular relaxation is constitutively specified by

$$\tilde{\mathbf{D}}^F_B = \dot{\gamma}^F_B \mathbf{N}_B, \tag{13}$$

where $\mathbf{N}_B$ is the normalized deviatoric portion of the network stress

$$\mathbf{N}_B = \frac{1}{\sqrt{2}\tau_B}\mathbf{T}'_B, \qquad \tau_B = \left[\tfrac{1}{2}\mathbf{T}'_B\mathbf{T}'_B\right]^{1/2}. \tag{14}$$

The scalar equivalent rate of relaxation, $\dot{\gamma}^F_B$, must now be prescribed. Here, the relaxation process is assumed to be one of chain reptation. Bergstrom and Boyce [16] proposed a constitutive model for relaxation via stress-assisted chain reptation based on the Doi and Edwards [20] theory of reptational motion of chain molecules. In a manner similar to the Bergstrom and Boyce approach, the rate of relaxation is taken to be

$$\dot{\gamma}^F_B = C\left(\frac{1}{\lambda_F - 1}\right)\tau_B, \tag{15}$$

where $\lambda_F = [\frac{1}{3}\mathrm{tr}(\mathbf{F}^F_B\mathbf{F}^{FT}_B)]^{1/2}$, and the temperature dependence of relaxation is captured in C

$$C = D\exp\left\{-\frac{Q}{RT}\right\} \tag{16}$$

This relation captures the essence of the behavior observed in Figs. 9 and 10. The modification of this basic framework necessary to capture the cessation of molecular relaxation upon reaching a specific level of network orientation is discussed in Section 3.2.3. Eqs. (1) and (10)–(16)

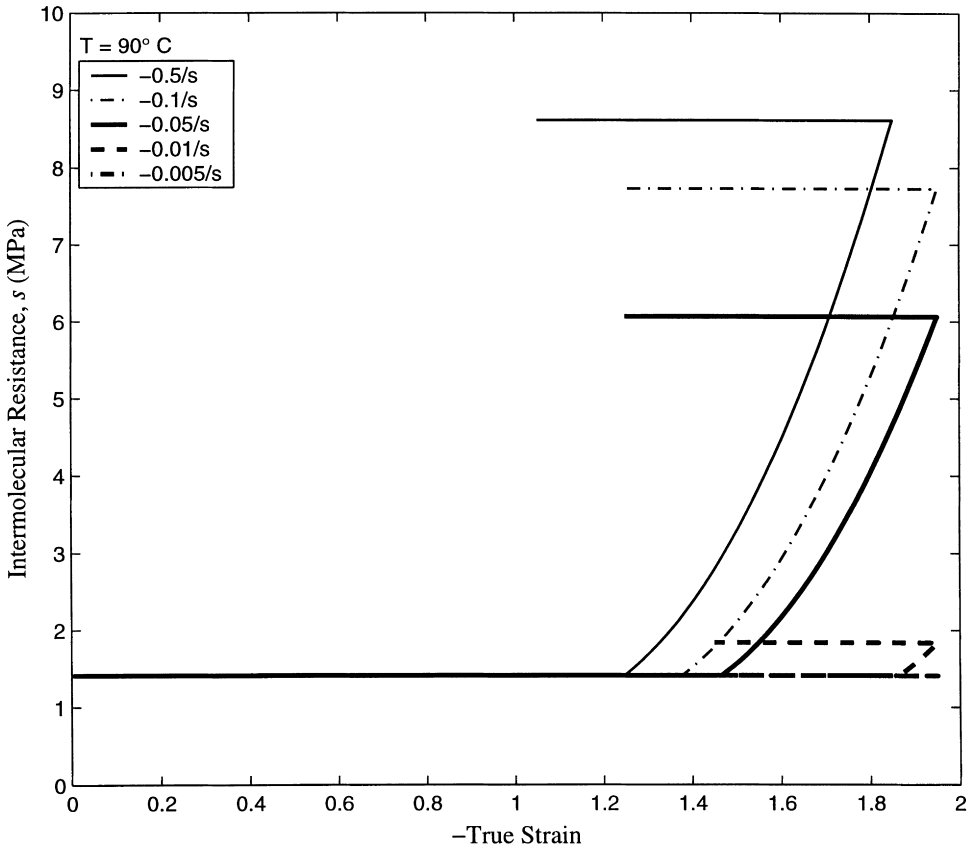

Fig. 13. Model predictions for the evolution of intermolecular resistance with applied strain, at 90°C in uniaxial compression.

completely describe the kinematic and constitutive aspects of resistance B.

The total stress acting on the system is then provided by

$$\mathbf{T} = \mathbf{T}_A + \mathbf{T}_B. \tag{17}$$

3.2.3. Strain-induced crystallization

As the PET is stretched, the underlying molecular network is oriented giving rise to resistance B as described in Section 3.2.2. Strain-induced crystallization is observed to initiate after a sufficient amount of molecular orientation has been achieved. Strain-induced crystallization has two major effects on the behavior: First, as shown in the data reduction of Figs. 9 and 10, molecular relaxation effectively ceases after a network stretch between 0.6 and 0.35 during uniaxial compression which correlates with the onset of crystallization (see [1,3]); second, the crystallization will alter the "intermolecular resistance" since it is no longer only amorphous domains which are deforming.

Effect on molecular relaxation. In Figs. 9 and 10, the flow stretch was observed to level off once the network stretch reached a magnitude between 0.6 and 0.35 in uniaxial compression, where the precise magnitude depends on rate and temperature. Converting the uniaxial stretch levels into effective chain stretches, molecular relaxation is found to cease at critical effective chain stretches $\bar{\lambda}_N$ between 1.05 and 1.35 depending on rate and temperature. At higher temperature and longer times, less molecular orientation (lower $\bar{\lambda}_N$) is needed to initiate crystallization as shown in Figs. 9 and 10. In order to account for the effect of strain-induced crystallization on the molecular relaxation process, Eq. (15) is modified

$$\dot{\gamma}_B^F = \begin{cases} C\left(\dfrac{1}{\lambda_F - 1}\right)\tau_B, & \bar{\lambda}_N < \bar{\lambda}_{NC}, \\ 0, & \lambda_N \geq \bar{\lambda}_{NC}, \end{cases} \tag{18}$$

where $\bar{\lambda}_{NC}$ is the critical network stretch which leads to the onset of crystallization and the cessation of molecular relaxation. The data provides a phenomenological expression for the rate and temperature dependence of $\bar{\lambda}_{NC}$

$$\bar{\lambda}_{NC} = \begin{cases} \lambda^*, & \dot{\gamma}_A^P < 0.0173\ s^{-1}, \\ \lambda^* + m\log(\dot{\gamma}_A^P/0.0173), & \dot{\gamma}_A^P > 0.0173\ s^{-1}, \end{cases} \tag{19}$$

where

$$\lambda^* = 1.25 - 0.02(\theta - 363\ \text{K}),$$

$$m = 0.05 + 0.01(\theta - 363\ \text{K}).$$

Effects on intermolecular resistance. Strain-induced crystallization results in an increase in percent crystalline domains and a corresponding decrease in percent

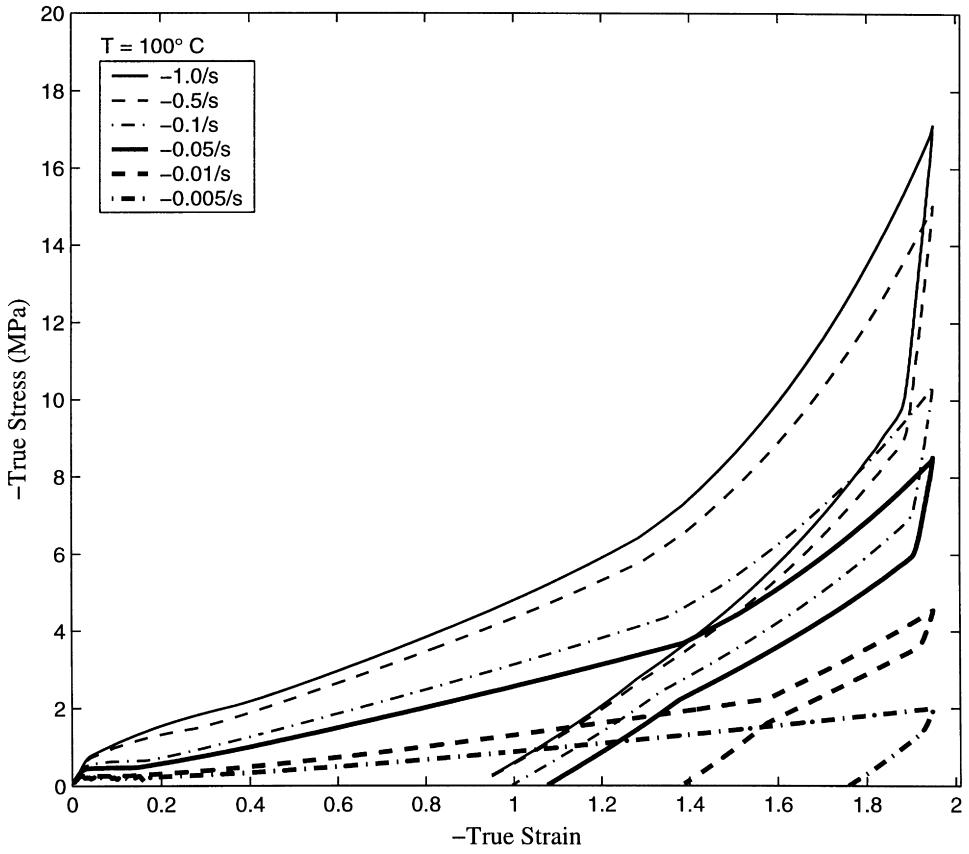

Fig. 14. Model predictions for the stress–strain behavior of PET at 100°C in uniaxial compression.

amorphous domains with strain. The size of crystallites which result from strain-induced crystallization are found to be small (<5 nm) (see [1,21]). Due to the small size of the crystallites, as a first approximation, the occurrence of crystallization can be considered to increase the effective isotropic resistance, s, to flow. This evolution in s will be modeled phenomenologically to increase with strain in a quadratic manner once $\bar{\lambda}_{NC}$ is reached. The baseline resistance s is temperature dependent and given by $s_0 = 0.15G$, where G is the temperature dependent shear modulus. Upon reaching the $\bar{\lambda}_N = 1.05\bar{\lambda}_{NC}$ condition, s will increase with strain due to crystallization. This increase is captured via an amplification factor α_s which evolves quadratically with network stretch during loading

$$d\alpha_s = \begin{cases} 0, & \bar{\lambda}_N < 1.05\bar{\lambda}_{NC}, \\ \dfrac{2A(\bar{\lambda}_N - 1.05\bar{\lambda}_{NC})}{(\sqrt{N} - 1.05\bar{\lambda}_{NC})^2}\, d\gamma, & \bar{\lambda}_N > 1.05\bar{\lambda}_{NC}, \end{cases} \tag{20}$$

$$\alpha_s = 1.0 + \int d\alpha_s,$$

$$s = \alpha_s s_0.$$

The shear modulus of "element A" is similarly amplified

$$G = \alpha_s G_0. \tag{21}$$

Note that in taking s to evolve in an isotropic manner, the model captures the main aspect of the change in structure from a soft amorphous structure to one where the resistance increases due to the evolution from amorphous to partly crystalline. In the WAXD data of Llana and Boyce [1], the crystallization was shown to occur in a highy textured (anisotropic) manner which indicates that s should evolve in an anisotropic manner. The anisotropic nature of s can be addressed in a future work.

4. Comparison of model and experiment results for isothermal loading cases

In this section, the ability of the constitutive model to capture and predict the strongly rate and temperature dependent material stress–strain behavior is examined by comparing simulations to experimental results. The material properties for the constitutive model are obtained by appropriately reducing the uniaxial compression data at different rates and temperatures. The data reduction procedure was discussed earlier in Section 2; the fitting of the model to the data is discussed in Appendix A.

The material properties were obtained primarily from the uniaxial compression data at 90°C, at strain rates of -0.5 and $-0.01\ s^{-1}$, and 100°C, at a strain rate of $-0.01\ s^{-1}$.

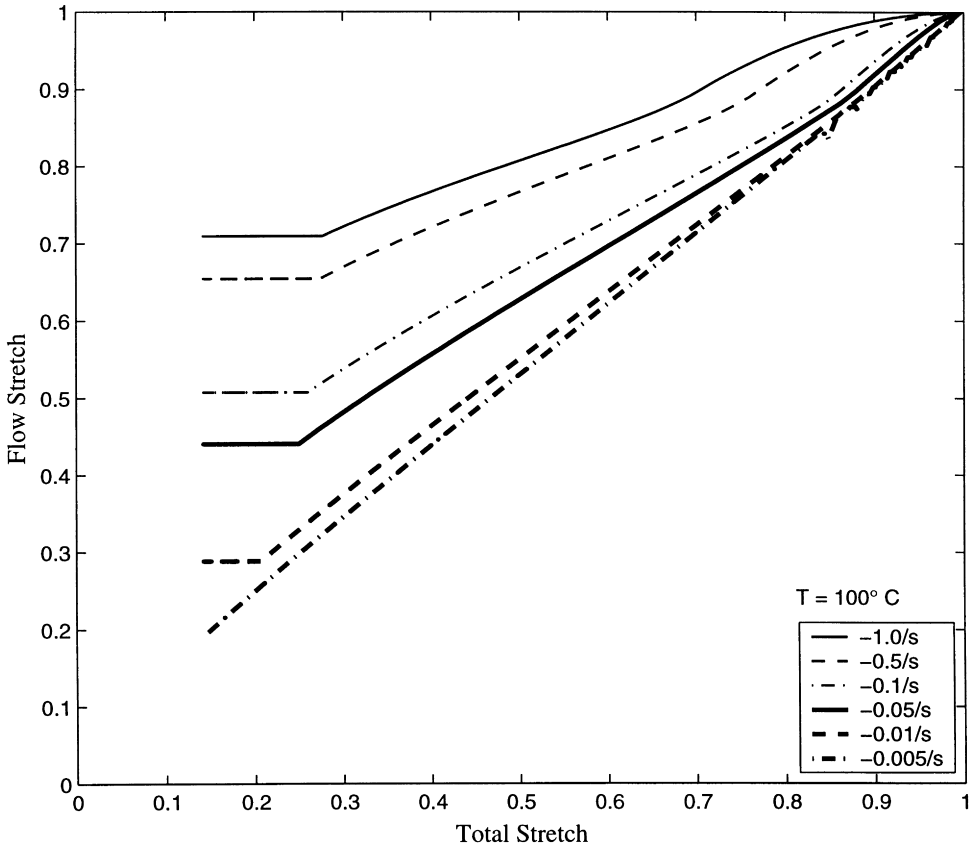

Fig. 15. Model predictions for the evolution of flow stretch with applied stretch at 100°C in uniaxial compression.

Reduction of these data provided the temperature dependence of the elastic properties $E_A(\theta)$; the initial flow properties $\dot{\gamma}_{0A}$, ΔG; the orientation hardening properties $nk\theta$, N; and the molecular relaxation properties D and Q. Unfortunately, the value of $\bar{\lambda}_{NC}$ associated with the onset of crystallization and the cessation of molecular relaxation was found to be strongly rate and temperature dependent; therefore, uniaxial compression data at 90 and 100°C at all strain rates was needed to fit this property. Future work will address the development of a more physical expression for this quantity (as opposed to the current phenomenological expression) which should limit the amount of data needed to fit this quantity.

Several loading conditions were simulated including uniaxial compression at various temperatures and strain rates as well as plane strain compression at various temperatures and strain rates.

4.1. Uniaxial compression simulation results

4.1.1. 90°C

Simulation results for uniaxial compression at 90°C at strain rates of -0.5, -0.1, -0.05, -0.01, and $-0.005\ s^{-1}$ are shown in Figs. 11–13. Fig. 11 depicts the prediction of the stress–strain behavior for the various rates and compares well with the data of Fig. 3. The initial flow stress increases with increase in strain rate, the initial hardening slope increases with an increase in strain rate, and the dramatic increase in hardening occurs earlier (at lower strains) with an increase in strain rate. The dependence of all of the basic characteristics of the stress–strain curve on strain rate are captured well; the stress–strain curve at each rate, while not precise, is in reasonably good agreement with the data.

The basic character of the unloading behavior is captured well where the initial unloading slope is relatively high followed by a transition to non-linear recovery. The model predicts a large amount of the imposed deformation to be retained upon unloading, consistent with the experimental data. We note that the unloading curves do not precisely capture the data, indicating a need for more research in this area. Modeling work of others (for example, Buckley and co-workers [4,15] and/or Vigny et al. [7]) only address the loading behavior and do not present unloading predictions.

The molecular relaxation process at each rate is examined in Fig. 12 where the axial flow stretch of resistance B is plotted as a function of applied stretch ($\lambda_{applied} = \exp(\varepsilon_{applied})$) for each rate. Relaxation is observed to be rate dependent, where more flow occurs at lower rates as evidenced by the continued decrease in flow stretch with applied stretch. This rate dependence of the evolution in

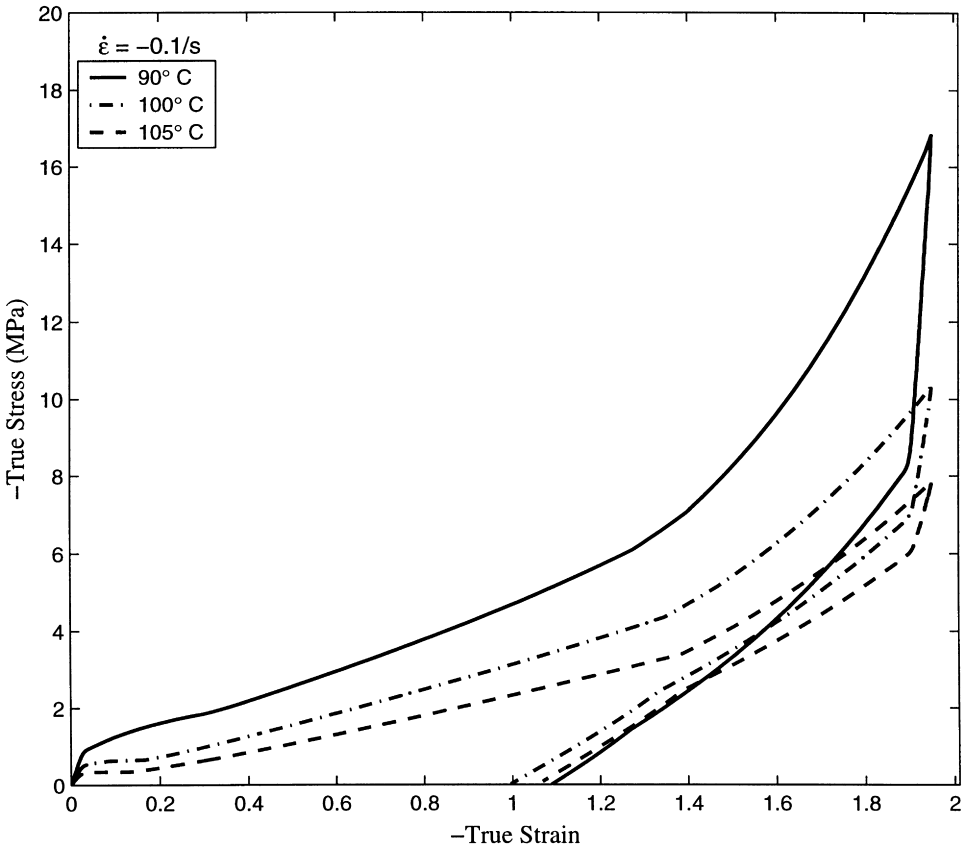

Fig. 16. Model predictions for the stress–strain behavior of PET at 90, 100, and 105°C in uniaxial compression at an applied strain rate of $-0.1\ s^{-1}$.

flow stretch with strain (molecular relaxation) is what leads to the rate dependence of the hardening slope observed in Fig. 12. The flow stretch is predicted to level off (i.e. molecular relaxation ceases) at an applied stretch level that depends on strain rate. These results compare reasonably well with the data reduction of Fig. 9(b).

The evolution of the intermolecular resistance *s* with applied strain during loading is depicted in Fig. 13 for each strain rate. The resistance *s* is observed to begin to increase at an applied strain that depends on the strain rate; this is due to more deformation going to orient the network at higher strain rates (as compared to the amount of deformation being accommodated by molecular relaxation) that in turn leads to crystallization beginning at lower strains. The increase in *s* with strain contributes to the strain hardening, but more importantly acts to hinder complete recovery of the material upon unloading. This feature of the model provided the reasonably good prediction of recovery behavior found in Fig. 11, when compared to the data in Fig. 2.

4.1.2. 100°C

Simulation results for uniaxial compression at 100°C at strain rates of -1.0, -0.5, -0.1, -0.05, -0.01, and $-0.005\ s^{-1}$ are shown in Figs. 14 and 15. Fig. 14 shows stress vs. strain; and Fig. 15 shows axial flow stretch (from molecular relaxation) vs. applied stretch. Comparison with the data of Fig. 2 shows good agreement with the stress–strain behavior, demonstrating the ability of the model to capture the temperature dependence of the material behavior and also the differences in the rate dependence at different temperatures. Comparison of Fig. 15 with Fig. 10(b) shows a good predication of molecular relaxation.

4.1.3. 90°C vs. 100°C vs. 105°C

Simulation results directly comparing the stress–strain behavior at 90, 100, and 105°C at a strain rate of $-0.1\ s^{-1}$ are shown in Fig. 16. The ability of the model to capture the strong temperature dependence is evident. The simulation results also compare favorably with the data of Fig. 4.

The uniaxial compression stress–strain simulation results demonstrate the ability of the constitutive model to capture and predict the many complicated temperature and strain rate dependent aspects of the behavior of PET at these temperatures.

4.2. Plane strain compression simulation results

Simulation results are presented for the case of plane strain compression at 100°C for the strain rates of -1.0,

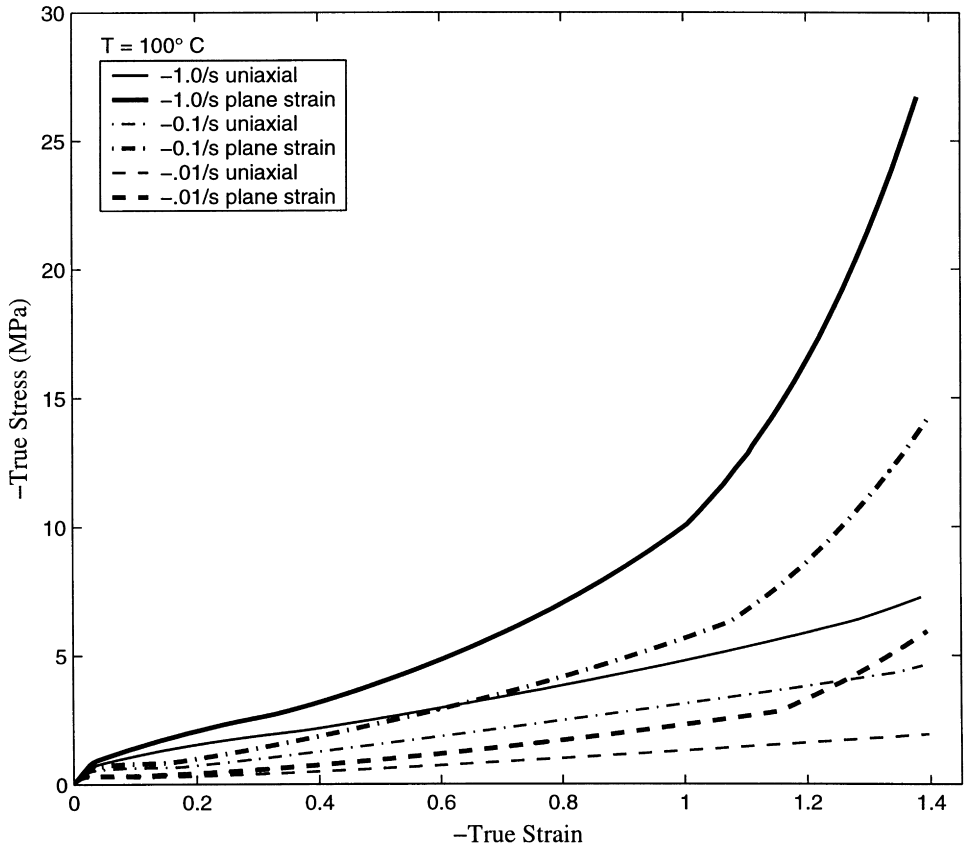

Fig. 17. Comparison of model predictions for the stress–strain behavior of PET at 100°C in uniaxial compression and in plane strain compression.

-0.1, and $-0.01\ s^{-1}$ in Fig. 17. The simulation results at 100°C for both plane strain compression and uniaxial compression are superposed for direct comparison to one another and can be compared to the data presented earlier in Fig. 5. The simulations are found to pick up the dramatic differences in the stress–strain behavior observed in plane strain compression vs. that observed in uniaxial compression. The first major difference is that the initial hardening slope is found to be much greater in plane strain compression than in uniaxial compression at any given strain rate; the plane strain hardening slope is well predicted for all rates. (Note that no plane strain data is used in the fitting of material constants.) The second major difference in plane strain compression vs. uniaxial compression is the much earlier occurrence of the "upturn" in the stress–strain behavior (the upturn occurs at lower strain in plane strain compression). The strain at which the upturn occurs is also very well predicted for all rates. The success of predicting the state of strain dependence of the initial hardening slope as well as the upturn lies in the model of molecular orientation being tied to the effective network stretch measure which evolves more rapidly with axial strain in plane strain compression than in uniaxial compression. The model clearly captures an incredibly wide range of loading conditions of practical interest, including strain states, strain rates, and temperatures.

5. Concluding remarks

A physically based, fully three-dimensional constitutive model for the strongly strain rate and temperature dependent stress–strain behavior of poly(ethylene terephthalate) at temperatures above the glass transition temperatures has been developed. The model is shown to successfully capture the key features of the stress strain behavior including:

- rate and temperature dependent initial flow stress;
- rate and temperature dependent strain hardening/stiffening modulus;
- rate and temperature dependent dramatic up-turn in the stress–strain behavior at large strains;
- state of strain dependence of (1) the initial flow stress, (2) the strain hardening/stiffening behavior, and (3) the up-turn in the stress–strain behavior.

The basic feature of the unloading behavior are also captured by the model although not as precisely as the loading response indicating a need for more research on this aspect of the behavior.

Acknowledgements

This research was funded by the National Science

Foundation through award numbers MSS-9215805 and CMS-9622526 and by the Eastman Kodak Company.

Appendix A. Determination of material properties

A.1. Intermolecular elastic properties

The experimentally observed initial stiffness has contributions from the elastic elements of both "A" and "B". However, we note that the initial modulus of "B" is approximately a factor of ten smaller than that of "A". Therefore, the initial slope of the stress–strain curve is used to determine the modulus of the elastic element of "A": E_A. E_A is temperature dependent

$$E_A(90°C) = 28 \text{ MPa},$$

$$E_A(100°C) = 16 \text{ MPa}.$$

The modulus at all other temperatures (at temperatures above 80°C) is obtained using a linear interpolation/extrapolation of the values for E_A at 90 and 100°C

$$E_A(\theta) = E_A(80°C) - m_E(\theta - 353 \text{ K}),$$

where $E_A(80°C) = 40 \times 10^6$ Pa and $m_E = 1.2 \times 10^6$ Pa/K.

No data was available for the Poisson ratio; given that the material is above the glass transition temperature, we take ν to be 0.49.

A.2. Intermolecular flow resistance

The inelastic strain rate which results after overcoming intermolecular barriers to flow was described by Eq. (9)

$$\dot{\gamma}_A^p = \dot{\gamma}_{0A} \exp\left[-\frac{\Delta G(1 - \tau_A/s)}{k\theta}\right].$$

The resistance s_0 is temperature dependent and simply modeled to be

$$s_0(\theta) = 0.15 G_A(\theta),$$

where $G_A = E_A/2(1 + \nu)$.

The material properties of $\dot{\gamma}_{0A}$ and ΔG of Eq. (9) are obtained by reducing the stress–strain data and obtaining the initial flow stress at a given temperature as a function of strain rate. Eq. (9) is then rearranged to read as the equation of a line

$$A \ln(\dot{\gamma}_A^p) - B = \left(\frac{1}{k\theta}\left(\frac{\tau}{s} - 1\right)\right),$$

where $A = 1/\Delta G$ and $B = A \ln \dot{\gamma}_{0A}$. The data pairs of shear flow stress and strain rate are then used to reduce values for A and B above, which in turn give the properties.

$$\dot{\gamma}_{0A} = 1.75 \times 10^6 \text{ s}^{-1},$$

$$\Delta G = 1.16 \times 10^{-19} \text{ J}.$$

A.3. Orientation hardening/stiffening

The orientation hardening/stiffening (the elastic element of "B") is described by Eq. (12)

$$\mathbf{T}_B = \frac{1}{J}\frac{n k\theta}{3}\frac{\sqrt{N}}{\bar{\lambda}_N}\mathcal{L}^{-1}\left[\frac{\bar{\lambda}_N}{\sqrt{N}}\right][\bar{\mathbf{B}}^N - (\bar{\lambda}_N)^2\mathbf{I}].$$

The material properties in this equation are $C_R = nk\theta$ which correlates with the initial hardening slope (of the 90°C, -0.5 s^{-1} data) and N which correlates with the effective stretch at which the upturn in the hardening behavior occurs (of the 90°C, -0.5 s^{-1} data). A fit to the 90°C, -0.5 s^{-1} uniaxial compression data gives

$$C_R = 2.10 \times 10^6 \text{ Pa},$$

$$N = 9.$$

A.4. Molecular relaxation

The flow due to molecular relaxation is described by Eqs. (15) and (16) as later limited due to strain-induced crystallization by Eq. (18).

$$\dot{\gamma}_B^F = C\left(\frac{1}{\lambda_B - 1}\right)\tau_B,$$

where the temperature dependence of relaxation is captured in C

$$C = D \exp\left\{-\frac{Q}{RT}\right\}.$$

The material properties that describe temperature dependent molecular relaxation are D and Q. These properties are obtained by obtaining a best fit for C at 90°C and C at 100°C through trial and error fit to the data at each temperature, at a strain rate of -0.01 s^{-1}. This procedure provided

$$C(90°C) = 0.63 \times 10^{-9} \text{ (Pa s)}^{-1},$$

$$C(100°C) = 4.0 \times 10^{-9} \text{ (Pa s)}^{-1}.$$

These values for C are then used to determine

$$D = 1.3 \times 10^{20} \text{ (Pa s)}^{-1},$$

$$Q/R = 24.5 \times 10^3 \text{ K},$$

or $Q = 2.036$ J/mol where R is the universal gas constant (8.31 J/mol K).

A.5. Strain-induced crystallization: effects on molecular relaxation

Strain-induced crystallization acts to halt molecular relaxation. The network stretch at which relaxation ceases, $\bar{\lambda}_{NC}$, is rate and temperature dependent as shown in the data of Figs.10(c), 11(c), and 12(c). An expression for the rate

and temperature dependence of $\bar{\lambda}_{NC}$ was phenomenologically obtained from this data and was given in Eq. (19).

A.6. Strain-induced crystallization: effects on intermolecular resistance

Upon $\bar{\lambda}_N$ reaching $\bar{\lambda}_{NC}$, the intermolecular resistance s is taken to monotonically increase with strain. This increase is captured via an amplification factor α_s which evolves with strain as described earlier in Eq. (20)

$$d\alpha_s = \begin{cases} 0, & \bar{\lambda}_N < 1.05\bar{\lambda}_{NC}, \\ \dfrac{2A(\bar{\lambda}_N - 1.05\bar{\lambda}_{NC})}{(\sqrt{N} - 0.95\bar{\lambda}_{NC})^2}\Delta\gamma, & \bar{\lambda}_N > 0.95\bar{\lambda}_{NC}, \end{cases}$$

$$\alpha_s = 1.0 + \int d\alpha_s.$$

This evolution equation provides for an approximately quadratic increase in α_s with strain. The additional material property introduced here is the dimensionless scale factor A, which determines the magnitude of the increase of α_s with strain. Fitting the data gave for A a value of 30.

References

[1] Llana PG, Boyce MC. Finite strain behavior of PET above the glass transition temperature. Polymer 1999;40:6729–51.

[2] Jabarin SA. Strain-induced crystallization of poly(ethylene terephthalate). Polym Engng Sci 1992;32:1341–9.

[3] Chandran P, Jabarin S. Biaxial orientation of poly(ethylene terephthalate) Part I: nature of the stress-strain curves. Adv Polym Technol 1993;12:119–32.

[4] Buckley CP, Jones DC, Jones DP. Hot-drawing of poly(ethylene terephthalate) under biaxial stress: application of a three-dimensional glass-rubber constitutive model. Polymer 1996;37:2403–14.

[5] Adams AM, Buckley CP, Jones DP. Biaxial, hot drawing of amorphous poly(ethylene terephthalate). Proceedings of the Ninth International Conference in Deformation, Yield and Fracture of Polymers, Cambridge, UK, 1994.

[6] Zaroulis JS, Boyce MC. Temperature, strain state and strain rate dependence of the evolution in mechanical behavior and structure of poly(ethylene terephthalate) with finite strain deformation. Polymer 1997;38:1303–15.

[7] Vigny M, Aubert A, Hiver JM, Aboulfaraj M, G'Sell C. Constitutive viscoplastic behavior of amorphous PET during plane strain tensile stretching. Polym Engng Sci 1999 submitted for publication.

[8] Arruda EM, Boyce MC. Evolution of plastic anisotropy in amorphous polymer during finite straining. Int J Plasticity 1993;9:697–720.

[9] Haward RN, Thackray G. The use of a mathematical model to describe isothermal stress-strain curves in glassy thermoplastics. Proc R Soc London, Ser A 1968;302:453.

[10] Boyce MC, Parks DM, Argon AS. Large inelastic deformation of glassy polymers. Part I: rate dependent constitutive model. Mech Mater 1988;7:15–33.

[11] Buckley CP, Jones DC. Glass-rubber constitutive model for amorphous polymers near the glass transition. Polymer 1995;36:3301–12.

[12] Zaroulis JS, Boyce MC. Mechanical behavior of poly(ethylene terephthalate) during large strain deformation. In: Boyce MC, editor. ASME MD Vol. 681 AMD Vol. 215, Mechanics of plastics and plastic composites, 1995.

[13] Edwards SF, Vilgis TH. The effect of entanglements in rubber elasticity. Polymer 1986;27:483–92.

[14] Arruda EM, Boyce MC, Jayachandran R. Effects of strain rate, temperature and thermo-mechanical coupling on the finite strain deformation of glassy polymers. Mech Mater 1995;19:193–212.

[15] Gerlach C, Buckley CP, Jones DP. Development of an integrated approach to modelling of polymer film orientation processes. Trans I Chem E, Part A 1998;76:38–44.

[16] Bergstrom JS, Boyce MC. Constitutive modelling of the large strain time dependent behavior of elastomers. J Mech Phys Solids 1998;46:931–57.

[17] Llana PG. The mechanics of strain induced crystallization in PET. S.M. Thesis, Massachusetts Institute of Technology, Department of Mechanical Engineering, Cambridge, MA, 1998.

[18] Boyce MC, Weber GG, Parks DM. On the kinematics of finite strain plasticity. J Mech Phys Solids 1989;37:647–65.

[19] Kocks VF, Argon AS, Ashby MF. Thermodynamics and kinetics of slip. Progress in material science, vol. 19. Oxford, UK: Pergamon Press, 1975.

[20] Doi M, Edwards MF. The theory of polymer dynamics, Oxford: Oxford University Press, 1986.

[21] Salem DR. Development of crystalline order during hot-drawing of PET film: influence of strain rate. Polymer 1992;33:3182–8.

[22] Arruda EM, Boyce MC. A three-dimensional constitutive model for the large stretch behavior of rubber–elastic materials. J Mech Phys Solids 1993;41:389–412.